Biophysical Journal
Article

Biophysical Society

Super-Resolution Imaging Reveals TCTN2 Depletion-Induced IFT88 Lumen Leakage and Ciliary Weakening

Rueyhung Roc Weng,[1] T. Tony Yang,[1] Chia-En Huang,[1] Chih-Wei Chang,[1] Won-Jing Wang,[2] and Jung-Chi Liao[1,3,*]

[1]Institute of Atomic and Molecular Sciences, Academia Sinica, Taipei, Taiwan; [2]Institute of Biochemistry and Molecular Biology, National Yang Ming University, Taipei, Taiwan; and [3]Genome and Systems Biology Degree Program, National Taiwan University, Taipei, Taiwan

ABSTRACT The primary cilium is an essential organelle mediating key signaling activities, such as sonic hedgehog signaling. The molecular composition of the ciliary compartment is distinct from that of the cytosol, with the transition zone (TZ) gated the ciliary base. The TZ is a packed and organized protein complex containing multiple ciliopathy-associated protein species. Tectonic 2 (TCTN2) is one of the TZ proteins in the vicinity of the ciliary membrane, and its mutation is associated with Meckel syndrome. Despite its importance in ciliopathies, the role of TCTN2 in ciliary structure and molecules remains unclear. Here, we created a CRISPR/Cas9 TCTN2 knockout human retinal pigment epithelial cell line and conducted quantitative analysis of geometric localization using both wide-field and super-resolution microscopy techniques. We found that TCTN2 depletion resulted in partial TZ damage, loss of ciliary membrane proteins, leakage of intraflagellar transport protein IFT88 toward the basal body lumen, and cilium shortening and curving. The basal body lumen occupancy of IFT88 was also observed in si-RPGRIP1L cells and cytochalasin-D-treated wild-type cells, suggesting varying lumen accessibility for intraflagellar transport proteins under different perturbed conditions. Our findings support two possible models for the lumen leakage of IFT88, i.e., a tip leakage model and a misregulation model. Together, our quantitative image analysis augmented by super-resolution microscopy facilitates the observation of structural destruction and molecular redistribution in *TCTN2*$^{-/-}$ cilia, shedding light on mechanistic understanding of TZ-protein-associated ciliopathies.

INTRODUCTION

The primary cilium serves as a hub mediating key signaling activities, including sonic hedgehog (Shh) signaling and PDGFα-signaling (1,2). It is a rod-shaped organelle originated from the mother centriole-converted basal body (BB). The backbone of the BB is a ring-shaped arrangement of nine microtubule triplets of ~180 nm diameter and 500 nm length, forming a highly sophisticated protein complex from the proximal end to the distal end and from the outer region to the lumen (3–6). The ciliary axoneme is nucleated from the distal end of the BB with nine microtubule doublets as its backbone (3,7). It is enveloped by the ciliary membrane, forming a cylindrical organelle at a diameter of ~240 nm and a length of ~2–5 μm. The microtubules of the BB and a large portion of the cilium are glutamylated, which is responsible for the regulation of microtubule severing (8); the microtubules of most of the cilium are acetylated, protecting microtubules from mechanical fatigue and increasing bending rigidity (9).

Ciliogenesis is initiated by the recruitment of key elements to the distal end of the BB, where the distal appendages (DAPs), including their associated proteins CEP164, SCLT1, and FBF1 (3,10), are located. Molecular motors, intraflagellar transport (IFT) proteins, ciliogenesis initiation kinase TTBK2, ciliary pocket protein EHD1, and ciliary vesicles are recruited to this region, prompting the removal of negative regulators such as CP110 capped at the centriole distal end. The transition zone (TZ) is then formed at the ciliary base interfacing the cytosol and the ciliary compartment (11,12). IFT is a bidirectional transport driven by molecular motors essential to carrying precursors for ciliogenesis (13,14).

Submitted February 2, 2018, and accepted for publication April 23, 2018.

*Correspondence: jcliao@iams.sinica.edu.tw

Rueyhung Roc Weng and T. Tony Yang contributed equally to this work.

Rueyhung Roc Weng's present address is Department of Internal Medicine, National Taiwan University Hospital, Taipei, Taiwan.

Chia-En Huang's present address is TFBS Bioscience, Inc., Taipei, Taiwan.

Editor: Julie Biteen.

https://doi.org/10.1016/j.bpj.2018.04.051

The TZ is another highly organized protein complex with Y-shaped linkers (Y-links) observed in electron microscopy (EM) bridging the axoneme and the ciliary membrane (15–27). CEP162 is an axoneme-associated protein localized at the ciliary base important for TZ assembly (28). RPGRIP1L serves as a core component essential for anchoring Meckel syndrome (MKS) and nephronophthisis (NPHP) modules (24). CEP290 is essential for Y-link formation and serves as a central assembly factor of the MKS module (26,29). Tectonic 1 (TCTN1) and Tectonic 2 (TCTN2) regulate ciliogenesis and Shh signaling (19,20,30,31). TZ localization of MKS1 and TMEM67 requires TCTN1, which also interacts with the NPHP module (19,32). Both TCTN1 and TCTN2 mutations result in the absence of ARL13B and the reduced abundance of smoothened (SMO) under SMO agonist treatment in cilia. Several TZ proteins have been shown to establish a diffusion barrier to regulate ciliary entry and exit (24,33–36). IFT proteins, axonemal precursors, receptors, ion channels, and other signaling molecules all have to pass through the TZ to enter the ciliary compartment for proper ciliogenesis and signaling (14,37). Specifically, ciliary localization of Shh signaling molecules, such as SMO, is affected by TZ mutation (19,21,30,38,39). We have mapped the molecular architecture of the TZ, showing that RPGRIP1L and CEP290 are close to the axoneme; TMEM67 and TCTN2 are close to the ciliary membrane, whereas MKS1 is likely in between (40).

Super-resolution imaging of the TZ by others and us has shown the molecular architecture of the TZ protein complex (27,40–42). Rings of TZ proteins were found disrupted with super-resolution imaging when RPGRIP1L was mutated (27). Localization of IFT88 relative to the TZ has also been shown by others and us (27,40). We have shown two different IFT88 distribution patterns under different growth conditions (43), illustrating the dynamic characteristics of IFT proteins. Despite the abovementioned studies, detailed effects on molecular distributions, such as IFT protein localization as well as axonemal structural feature, remain elusive. Specifically, will damage of the TZ structure cause axonemal structural collapse, traffic jams, or structural breaks? Would IFT proteins maintain their molecular distribution when the TZ malfunctions? It will be important to see the changes of IFT protein localization when the TZ is damaged to better understand the roles of TZ proteins.

MATERIALS AND METHODS

Antibodies and siRNA

Primary antibodies used in this study include anti-ARL13B (ab136648, 1:500 dilution), acetylated tubulin (AcTub, ab24610, 1:1000 dilution), SMO (ab38686, 1:500 dilution), EHD1 (ab109311, 1:500 dilution), TCTN2 (ab119091, 1:200 dilution), CEP290 (ab84870, 1:200 dilution), IFT88 (ab42497, 1:200 dilution) (Abcam, Cambridge, MA), TMEM67 (13975-1-AP, 1:200 dilution), IFT88 (13967-1-AP, 1:200 dilution), MKS1 (16206-1-AP, 1:100 dilution), RPGRIP1L (55160-1-AP, 1:200 dilution), NPHP4 (13812-1-AP, 1:200 dilution), CP110 (12780-1-AP, 1:200 dilution), FBF1 (11531-1-AP, 1:500 dilution), IFT144 (ab13647, 1:100 dilution) (Proteintech Group, Chicago, IL), CEP164 (sc-240226, 1:200 dilution; Santa Cruz Biotechnology, Santa Cruz, CA), GAPDH (2118s, 1:2000 dilution), β-actin (3700 s, 1:2000 dilution) (Cell Signaling Technology, Danvers, MA), polyglutamylated tubulin (GT335, AG-20B-0020-C100, 1:1000 dilution; AdipoGen, San Diego, CA), CEP162 (HPA030170, 1:500 dilution), TTBK2 (HPA018113, 1:1000 dilution) (Sigma Aldrich, St. Louis, MO), and SCLT1 (a gift from Bryan Tsou, Sloan Kettering Institute (10), 1:200 dilution).

Synthetic small interfering RNA (siRNA) oligonucleotides were acquired from Dharmacon (ON-TARGETPlus SMART pool siRNA; Thermo Fisher Scientific, Waltham, MA). The 19-nucleotide siRNA sequences targeting TCTN2 corresponded to 5′-TCACGCTCCAGTCTTCCGT-3′, 5′-TGAGTCGCTTGTATTAATG-3′, 5′-TCGTTCTTGGTATAGTTCC-3′, and 5′-TTTCGAGCCAGCCATCACT-3′. The 19-nucleotide siRNA sequences targeting RPGRIP1L corresponded to 5′-TTAATCGGAACCAGTATTC-3′, 5′-TCATTAACTAGCCGTATTA-3′, 5′-TAATTCTATCCTGCAGCTC-3′, and 5′-ATCCACGAAAGATACCTTC-3′. The 19-nucleotide siRNA sequences targeting scrambled sequences corresponded to 5′-TTAGTCGACATGTAAACCA-3′, 5′-TCACACAACATGTAAACCA-3′, 5′-TCAGAAAACATGTAAACCA-3′, and 5′-TAGGAAAACATGTAAACCA-3′, which were used as negative controls.

Cell culture and transfection

The hTERT human retinal pigment epithelial cells (RPE1, CRL-4000; American Type Culture Collection, Manassas, VA) were maintained in Dulbecco's modified Eagle medium/F-12 (1:1) medium supplemented with 10% fetal bovine serum (FBS) and 1% penicillin-streptomycin. To induce ciliogenesis, cells at 70% confluence were starved with the FBS-free medium for 48 h. Transiently exogenous overexpression of full length TCTN2 and depletion of endogenous TCTN2 and RPGRIP1L proteins were achieved by introducing pBudCE4.1-TCTN2 plasmid and siRNA, respectively, with Lipofectamine 3000 and RNAiMAX reagents according to the manufacturer's suggestion (Thermo Fisher Scientific). Permanent expression of various truncated TCTN2 proteins in TCTN2-KO RPE1 cells was performed using a tetracycline-inducible lentiviral expression system with pLVX-tight-puro vector (Clontech, Mountain View, CA). For the cytochalasin D (Cyto D, 200 nM) treatment, cells that have been starved for 28 h were subject to Cyto-D-containing FBS-free medium for 20 h.

CRISPR/Cas9-mediated genome editing of RPE1 cells

Editing of the *TCTN2* locus in RPE1 cells was achieved through coexpression of the Cas9 protein with *TCTN2*-targeting guide RNA (gRNA) (44). The sequence (5′-GGTGGAAGAGAGGTCTGGAC-3′) of the gRNA-targeting site of *TCTN2* was obtained using the *E-CRISP* tool (45). Primer pairs carrying the target sequence were annealed and extended to generate a 100 bp double-strain DNA fragment using Phusion DNA polymerase (New England Biolabs, Ipswich, MA). *TCTN2* gRNA expressing plasmid was created by incorporating the amplicon into an *AflII*-linearized gRNA cloning vector (plasmid #41824; Addgene, Cambridge, MA; deposited by G. Church) using the Gibson assembly approach (New England BioLabs), as described previously (44). For cotransfection, the resulting gRNA cloning vector and Cas9-expressing plasmid (plasmid #41815; Addgene; deposited by G. Church) were complexed with *jetPRIME* reagent (Polyplus Transfection, New York, NY) and added to RPE1 cells at 80% confluence. Pure TCTN2 knockout (KO) cell lines were then established through clonal propagation from single cells, which lost the TCTN2 protein expression validated by immunofluorescence and immunoblotting with anti-TCTN2

antibody. To validate the mutation of the *TCTN2* genomic locus of the KO lines, the gRNA-targeted region was cloned into plasmid pBudCE4.1 (Thermo Fisher Scientific) and subjected to Sanger sequencing. FBF1 KO RPE1 lines were acquired as described previously (46).

Immunofluorescence labeling and imaging

Cells grown on poly-L-lysine-coated glass coverslips were fixed for 10 min with ice-cold methanol or 4% (w/v) paraformaldehyde in phosphate-buffered saline (PBS) depending on the suggested conditions for each antibody. Fixed cells were permeabilized for 10 min in PBS containing 0.1% Triton X-100 (PBST) and blocked with 3% (w/v) bovine serum albumin in PBST. Subsequently, cells were incubated with primary antibodies diluted in the blocking solution for 1 h at room temperature, followed by washing with PBST three times. Fluorescently labeled secondary antibodies were then carried out in blocking buffer for 1 h at room temperature. After three washes with PBST, cell nuclei were stained with Hoechst 33342 (Thermo Fisher Scientific) in PBS. Finally, the coverslips were washed with PBS and mounted on microscope slides with VECTASHIELD mounting medium (Vector Laboratories, Burlingame, CA). Cell imaging was performed using an epifluorescence microscope (IX81; Olympus Corporation, Tokyo, Japan). All statistical analyses in figures were reported as mean ± SD except Fig. 1 *G*, where the box and whisker plot was used to show the median and 10–90 percentile values.

Super-resolution imaging and analysis

dSTORM (direct stochastic optical reconstruction microscopy) imaging was performed on a modified inverted microscope (Eclipse Ti-E; Nikon, Tokyo, Japan). Two excitation lasers (OBIS 637 LX 140 mW, Coherent, Santa Clara, CA; and Jive 561 150 mW, Cobolt, Solna, Sweden) and an activation laser (OBIS 405 LX 100 mW; Coherent) were merged and homogenized (Borealis Conditioning Unit, Spectral Applied Research, Toronto, Canada) before focused on the back aperture of an objective (100× 1.49 NA Apo total internal reflection fluorescence; Nikon). A perfect focusing system (Nikon) was utilized to stabilize the z axis position. The excitation lights were operated at an intensity of ~3 kW/cm^2 for efficient conversion of the fluorophores to the dark state. A weak 405 nm light (~W/cm^2) was used to activate a fraction of the fluorophores returning to the excited state. The fluorescence signals emitted from individual fluorophores were filtered and imaged onto an electron-multiplying charge-coupled device (Evolve 512 Delta; Photometrics, Tucson, AZ). 10,000–20,000 sequential images were acquired with an exposure time of 20 ms. Fiducial markers (Tetraspeck; Thermo Fisher) coated on samples were recorded for postcorrection of drifting. Individual single-molecule peaks were then real-time detected using a MetaMorph super-resolution module (Molecular Devices, Sunnyvale, CA) based on a wavelet segmentation analysis. For two-color imaging, a sequential recording was performed by first imaging Alexa Fluor 647, followed by Cy3B. The super-resolution data were cleaned with a Gaussian filter with a radius of 0.8−1 pixel.

During the acquisition of dSTORM imaging, samples were incubated in an imaging buffer containing Tris-HCl/NaCl buffer at pH 8.0 and an oxygen-scavenging system consisting of 60−100 mM mercaptoethylamine at pH 8.0, 0.5 mg/mL glucose oxidase, 40 μg/mL catalase, and 10% (w/v) glucose (Sigma-Aldrich). Lateral position drift was compensated by aligning fiducial markers with ImageJ, and the chromatic aberration between Alexa 647 and Cy3B channels was corrected with a homemade algorithm relocating each pixel of a 561 nm image to its targeted position in the 647 nm channel.

To compare the longitudinal distribution of IFT88, SCLT1 was used as a reference to align each image. To determine the lateral width of the IFT88 distribution, the lateral profile was extracted at each longitudinal position and then fitted either by a Gaussian function or a double Gaussian mixed model. The width indicated in the data set was estimated based on the full width at half-maximum (FWHM) of a single Gaussian distribution, i.e., 2.354c (c, SD), for a single peak distribution or the effective FWHM of a mixed Gaussian function, 2.354(c1+c2)/2 (c1 and c2, SDs), for a two-peak pattern.

To measure the curvature of cilia, a segment of a cilium proximal of the maximal curved region was fitted with three arbitrary points that passed through the midline of the cilium. The maximal curvature k was then calculated according to a three-point fitting circle with a radius of $1/k$. To estimate the tapering angle, each cilium image was first straightened with ImageJ (straighten function), and the angle was defined by the two boundaries of GT335 signals.

Immunoblotting

Whole cell extracts were prepared by lysing cells with radio immunoprecipitation assay lysis buffer (50 mM Tris-HCl at pH 7.4, 150 mM NaCl, 0.25% deoxycholic acid, 1% NP-40, 1 mM EDTA) after PBS washing. Final 10 mM phenylmethylsulfonyl fluoride and 1× Halt protease/phosphatase inhibitor cocktails (Thermo Fisher Scientific) were freshly added into radio immunoprecipitation assay lysis buffer before use. After vortex, lysates were centrifuged at 14,000 × g for 15 min to remove debris. Protein concentration was determined by a DC Protein Assay kit (Bio-Rad, Hercules, CA). Protein samples were boiled in 1× Laemmli loading buffer (Bio-Rad) supplemented with 10% 2-mercaptoethanol, resolved with sodium dodecyl sulfate polyacrylamide gel electrophoresis gel, and transferred onto the polyvinylidene fluoride membrane. The membrane was blocked with 5% nonfat dry milk before hybridization with primary antibodies, followed by horseradish-peroxidase-conjugated secondary antibodies. Protein signals were detected using Luminata Crescendo Western horseradish peroxidase substrate (Millipore, Billerica, MA).

We used the lysates from both TCTN2 siRNA-treated and wild-type TCTN2 overexpressed RPE1 cells to verify the TCTN2 antibody specificity in the immunoblotting analysis. The result allowed us to screen TCTN2 KO mutants using the immunoblotting assay with the TCTN2 antibody.

Transmission EM

RPE1 cells grown and starved on Aclar film (Electron Microscopy Sciences, Hatfield, PA) were fixed with solution containing 4% paraformaldehyde and 2.5% glutaraldehyde with 0.1% tannic acid in 0.1 M sodium cacodylate buffer at room temperature for 30 min. After postfixation with 1% OsO4 in sodium cacodylate buffer for 30 min on ice, the cell blocks were dehydrated in a graded series of ethanol and infiltrated/embedded in EPON812 resin (Electron Microscopy Sciences). The resin blocks were incised on a microtome (Ultracut UC6; Leica, Wetzlar, Germany) to generate serial sections with ~90 nm thickness. Samples were stained with 1% uranyl acetate and 1% lead citrate and examined on a transmission EM (Philips CM100; Field Electron and Ion Company, Hillsboro, OR).

RESULTS

CRISPR/Cas9 KO of *TCTN2* partially damages the TZ

To understand the role of TCTN2 in the formation of human primary cilia, we used CRISPR/Cas9-mediated genome editing to generate an in-frame deletion of *TCTN2* in RPE1 cells. No TCTN2 signal was observed in immunostained images of the *TCTN2*-deficient mutant, or *TCTN2*$^{-/-}$ (Fig. 1 *A*), and immunoblotting also confirmed the effectiveness of the *TCTN2* KO (Fig. S1 *A*). A sequence analysis showed a single-base frame shift, resulting in

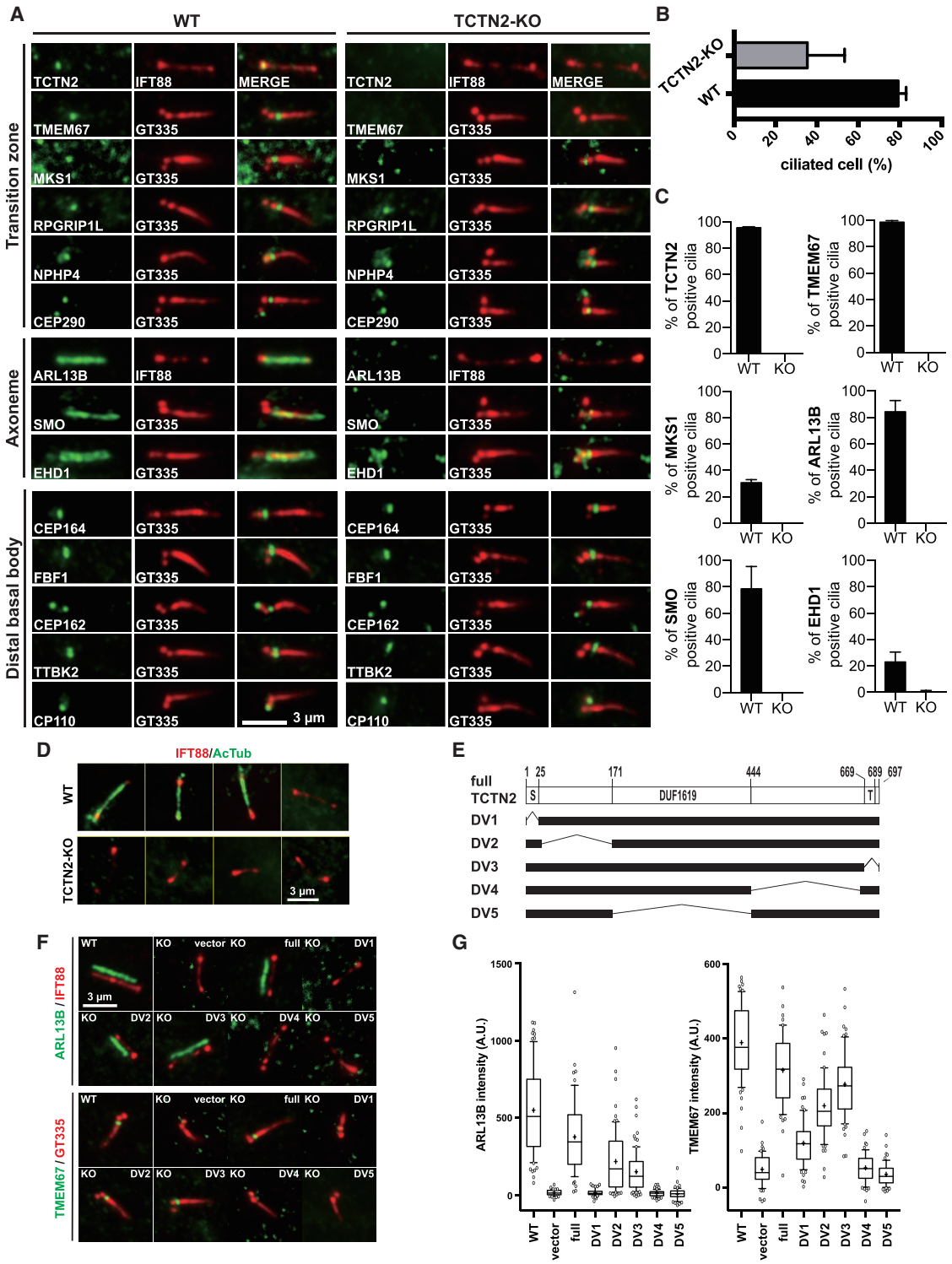

FIGURE 1 Transition zone (TZ) damage and loss of ciliary membrane protein retention due to TCTN2 depletion. (*A*) Immunofluorescence examination of ciliary proteins of starved wild-type (WT) and TCTN2-KO RPE1 cells is shown. Cilia are shown with IFT88 or polyglutamylated tubulin (GT335) markers. (*B*) The percentages of ciliated cells show that TCTN2 depletion impairs cilia formation. (N = 3 and n > 300) (*C*) Statistics show the disappearance of TZ proteins TMEM67 and MKS1 as well as membrane proteins ARL13B, SMO, and EHD1 in *TCTN2*$^{-/-}$ cilia. (N = 3 and n > 100) (*D*) The absence of acetylated tubulin in *TCTN2*$^{-/-}$ cilia is indicated. (*E*) A graph illustrates the different deletion variants (DVs) and their corresponding domains of TCTN2 proteins (S, putative ciliary targeting sequence; T, transmembrane motif). (*F*) Rescue of ARL13B ciliary retention and TMEM67 localization by ectopic expression of full, DV2, and DV3 fragments are shown. (*G*) Statistics of data in (*F*) (n > 50) are shown. To see this figure in color, go online.

premature stop and a mutated *TCTN2* homogenous allele that encoded a truncated TCTN2 comprising a 595 amino acid deletion and a 46 amino acid insertion at the C-terminal end (Fig. S1 *B*).

TCTN2$^{-/-}$ RPE1 cells showed a reduced ciliation frequency after 48 h of serum starvation (Fig. 1 *B*). Among the ciliated population, TMEM67 and MKS1 were absent in *TCTN2*$^{-/-}$ cells, whereas RPGRIP1L, NPHP4, and CEP290 remained in their ciliary base localizations (Fig. 1, *A* and *C*). That is, the TZ was partially damaged when TCTN2 was depleted, which was consistent with the previous findings in *TCTN1*$^{-/-}$ mouse embryonic fibroblasts (MEFs) (19). Considering this partial damage on the TZ structural framework that we obtained using super-resolution microscopy (40), it was suggested that depletion of the membrane-vicinal TCTN2 only locally destabilized the transmembrane protein TMEM67 and a middle region (presumably Y-link-associated) MKS1 but did not extend the damage to axoneme-vicinal CEP290 and RPGRIP1L. A surprising finding was that acetylated tubulin (AcTub) could not be observed in *TCTN2*$^{-/-}$ cilia (Fig. 1 *D*), suggesting that the acetylation process might be abolished by the TZ damage.

TCTN2 is required for the homeostasis of ciliary membrane proteins

Besides the impaired TZ, ciliary localization of membrane proteins including ARL13B (a small GTPase important for cilia formation (47,48)), SMO (an Shh-signaling-associated receptor (49)), and EHD1 (a ciliary pocket protein important for ciliogenesis in the early stage (50)) was also defective (Fig. 1 *A*). No ARL13B-enriched cilium was found in *TCTN2*$^{-/-}$ mutants (Fig. 1 *C*). Similarly, the SMO signal was very dim and considered absent in the axoneme of *TCTN2*$^{-/-}$ cilia upon SMO-agonist-stimulation. About 20% of the ciliated cells in the wild-type (WT) RPE1 showed retained EHD1 in mature cilia after 48 h starvation. However, almost no EHD1-positive cilia were observed in the *TCTN2*$^{-/-}$ cells. Previous studies showed that EHD1 is a direct binding partner of SMO and cotraffics with SMO into the developing primary cilia (51). Together with these observations, it is indicated that depletion of TCTN2 might lead to suppressed Shh response by impairing localization and enrichment of ciliary membrane proteins. Thus, TCTN2 is required for the homeostasis of ciliary membrane proteins.

Unlike the TZ and ciliary membrane compartments, protein components of DAPs were unaltered in the *TCTN2*$^{-/-}$ mutants (Fig. 1 *A*). Localizations of DAP proteins CEP164 and FBF1 as well as centriolar distal end protein CEP162 were not influenced by the depletion of TCTN2. In addition, the ciliogenesis-initiating kinase TTBK2 was enriched, and the ciliogenesis negative regulator CP110 was absent in the *TCTN2*$^{-/-}$ mutants; the same result was found in the WT cells. That is, the low ciliation frequency of *TCTN2*$^{-/-}$ mutants is not the outcome of impaired ciliogenesis initiation.

The N-terminal, the DUF1619 domain, and the C-terminal of TCTN2 are essential for TZ integrity and ciliary membrane protein retention

To gain insight into the functional domains of TCTN2 controlling TZ protein recruitment and ciliary membrane protein enrichment, we created multiple TCTN2 fragments and tested their effects. Protein BLAST search suggests that human TCTN2 contains a ciliary targeting sequence in the N-terminal and a cysteine-rich DUF1619 domain. We created five cell lines with domain variants (DVs) of TCTN2 stably expressed in the *TCTN2*$^{-/-}$ cells to examine whether they were necessary for TCTN2 functions (Fig. 1 *E*). Compared to the obvious rescuing effects on the recruitment of ARL13B and TMEM67 to cilia by expressing full-length TCTN2, DV1 lacking the N-terminal signal peptide failed to rescue the reduced ARL13B and TMEM67 signals (Fig. 1, *F* and *G*). This suggests that the N-terminal signal peptide is required for proper functions, potentially because of its signature for ciliary localization of TCTN2. Both DV4 lacking the C-terminal and DV5 lacking the DUF1619 domain were also unable to restore ARL13B and TMEM67 distributions at TCTN2-deficient cilia, suggesting that the C-terminal and the DUF1619 domain are indispensable for normal TCTN2 functions, similar to their essential roles for TCTN1 (19). By contrast, both expression of DV2, which lacks the nonconserved N-terminal segment, and DV3, which lacks the predicted transmembrane domain, were able to at least partially recover ciliary localization of ARL13B and TMEM67 (Fig. 1, *F* and *G*). Therefore, these two segments are not essential for TZ integrity and ciliary gating. Besides, although the TZ architecture revealed by stimulated emission depletion super-resolution imaging showed that TCTN2 is in the proximity of transmembrane TMEM67 (40) and that the predicted transmembrane domain of TCTN2 is not essential for TZ localization of the other transmembrane protein TMEM67.

TZ destruction results in IFT protein leakage toward the BB

To see how TCTN2 depletion-induced TZ destruction affected IFT, we examined the localization of IFT88 in WT and *TCTN2*$^{-/-}$ cells. By using IFT88 as a cilium marker to estimate the ciliary length, we found that ciliated *TCTN2*$^{-/-}$ cells had their cilia shorter than those in WT RPE1 cells (Fig. 2, *A* and *B*). In rare cases, extremely long IFT88-marked cilia could be observed in *TCTN2*$^{-/-}$ mutants. A large population of *TCTN2*$^{-/-}$ cells that grew cilia possessed a swelling tip of IFT88 (Fig. 2, *A* and *C*). The large variation in ciliary length and the tip accumulation

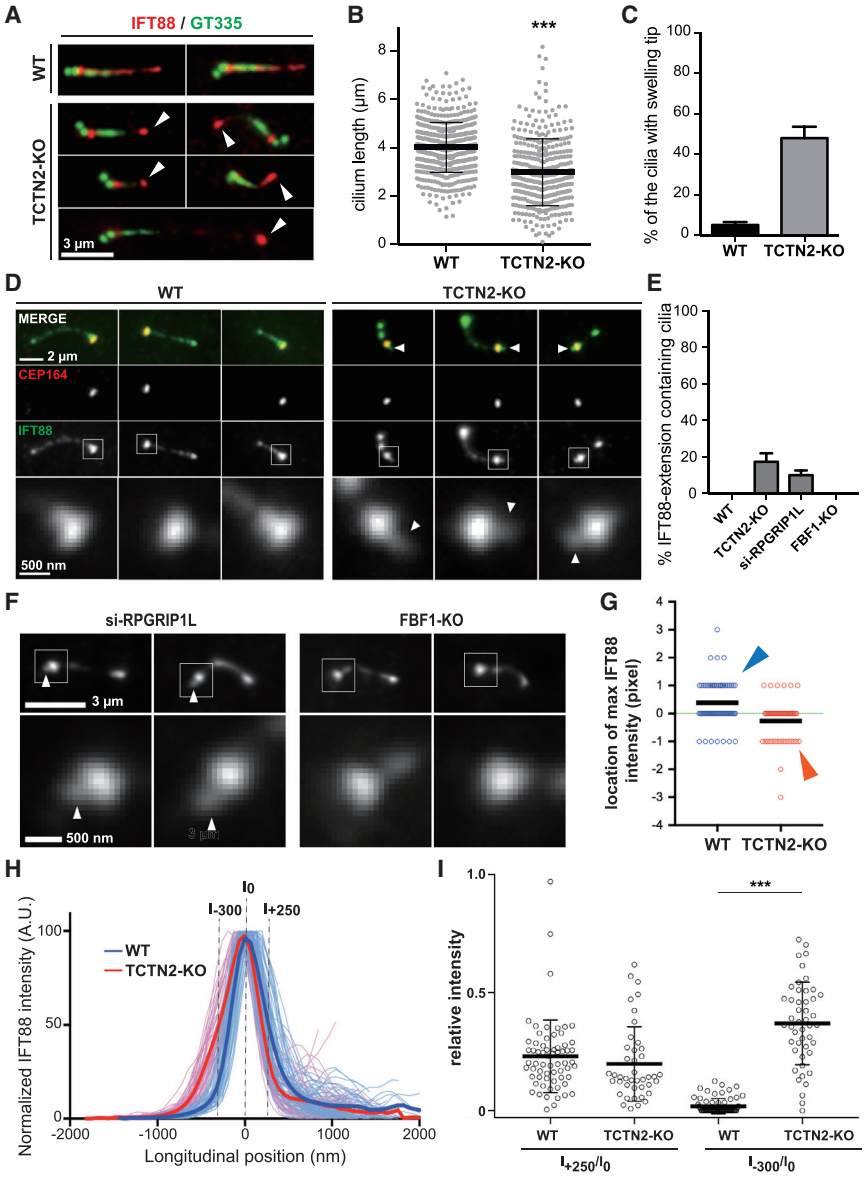

FIGURE 2 IFT88 extension toward the basal body (BB) due to TCTN2 depletion. (*A*) TCTN2 KO results in short and curved cilia with swelling tips of accumulated IFT88 molecules (*white arrowheads*). In rare cases, *TCTN2*$^{-/-}$ cilia are very long. (*B*) Statistics of cilium length show shortening of *TCTN2*$^{-/-}$ cilia ($n > 300$, $^{***}p < 0.001$ with unpaired *t*-test). (*C*) The population of cilia contains a swelling tip ($N = 3$ and $n > 100$). (*D*) IFT88 extension toward the BB in *TCTN2*$^{-/-}$ cells is shown (*white arrowheads* in enlarged graphs of the cilia base). (*E*) Statistics show the populations of cells with IFT88 extension toward the BB ($N = 3$ and $n > 100$). (*F*) The presence of IFT extension (*white arrowheads*) is shown in RPGRIP1L knockdown cells as well as the absence in FBF1 KO cells. (*G*) Positions of the maximal intensities of IFT88 epifluorescence signals are shown after aligning the locations of the maximal intensities of CEP164 as the origin (*green line*). The positive direction is the direction toward the ciliary tip. The result shows a population shift from the distal site of CEP164 (*blue arrowhead*) toward the BB direction upon TCTN2 depletion (*red arrowhead*). (*H*) Profiles show normalized IFT88 intensities (*thin lines*) and the average normalized intensity of all cilia (*thick lines*). I_0 indicates the CEP164 origin line as described in (*G*). The positive direction is the direction toward the ciliary tip. (*I*) Relative IFT88 intensities at I_{+250} and I_{-300} are compared to I_0 for each cilium shown in (*H*) ($^{***}p < 0.001$ with unpaired *t*-test). To see this figure in color, go online.

of IFT88 in *TCTN2*$^{-/-}$ cells were possibly due to aberrant gating at the TZ.

In close observation of IFT88 distributions, we found a surprising "tailed" pattern in *TCTN2*$^{-/-}$ cilia (Fig. 2 *D*, *arrowheads*; Fig. 2 *E*). Specifically, one could see a comet-like extension of IFT88 toward the BB in *TCTN2*$^{-/-}$ cells that was absent in WT cells (Fig. 2 *D*). This unexpected extension of IFT88 in *TCTN2*$^{-/-}$ cells was proximal of the wide region of IFT88, equivalently the DAP region, suggesting that IFT88 recruited by the DAPs not only had an accumulated tip population but also a BB population. To check whether the proximal extension of IFT88 was TCTN2 specific, we examined the IFT88 distributions in other perturbed cells. We found a similar IFT88 leakage toward the BB when knocking down RPGRIP1L, another TZ protein essential for supporting other TZ proteins (Fig. 2, *E* and *F*; Fig. S2, *A* and *B*) (24). In contrast, in ciliated cells of CRISPR/Cas9 KO of FBF1, a DAP protein not essential for ciliogenesis (10), we did not find the same leakage pattern for IFT88 in the BB (Fig. 2, *E* and *F*; Fig. S2, *A* and *B*). Therefore, these results revealed that TZ impairment by either depleting TCTN2 or RPGRIP1L induced mislocalization of IFT88 toward the BB.

We noticed that the IFT88 extension seemed to be restricted in space and length. To further ascertain the subciliary localization and distribution of IFT88 extension, we used DAP protein CEP164 as a longitudinal reference to evaluate the relative position of the extension. For both WT and *TCTN2*$^{-/-}$ cilia, the locations of maximal CEP164 intensities were aligned as the origin, and the

locations of maximal IFT88 intensities were plotted, showing longitudinal location differences of IFT88 between WT and *TCTN2*$^{-/-}$ cilia (Fig. 2 *G*). Normalizing maximal IFT88 intensities of each cilium, we were able to see similar trends of molecular distributions among WT cells as well as among *TCTN2*$^{-/-}$ cells (Fig. 2 *H*). IFT88 signals proximal of CEP164 (longitudinal position at −600 to −200) in *TCTN2*$^{-/-}$ cells were higher than those in WT cells. This result is consistent with the observation of IFT88 extension toward the BB in *TCTN2*$^{-/-}$ cells. The location of half-maximal intensity of *TCTN2*$^{-/-}$ cilia is ∼300 nm proximal of the origin (x = −300 nm). The intensity ratio of I_{-300}/I_0, i.e., the relative intensity between the origin and x = −300 nm, was another measure to show the statistical significance of BB leakage of IFT88 in *TCTN2*$^{-/-}$ cells (Fig. 2 *I*). According to our previous super-resolution imaging result (40), the distance between the TZ and CEP164 is around 250 nm. Therefore, to evaluate whether IFT88 accumulation will be observed at the TZ of *TCTN2*$^{-/-}$, we examined IFT88 signal at longitudinal position +250 nm (Fig. 2, *H* and *I*). We found a slight trend difference of IFT88 signals in the region distal of CEP164 (longitudinal position at +200 to +600) (Fig. 2 *H*), although it was statistically insignificant (Fig. 2 *I*).

dSTORM super-resolution imaging shows leakage of IFT88 into the BB lumen at the *TCTN2*$^{-/-}$ ciliary base

To further characterize the length and width of IFT88 extension in *TCTN2*$^{-/-}$ cells, we used dSTORM to further resolve IFT88 distributions in detail. We performed dual-color dSTORM super-resolution imaging of IFT88 and SCLT1, a DAP protein serving as a longitudinal position reference, in WT, *TCTN2*$^{-/-}$, and *FBF1*$^{-/-}$ RPE1 cells. Consistent with wide-field observation, we found an extension of IFT88 localization toward the BB in *TCTN2*$^{-/-}$; no such extension was observed in WT and *FBF1*$^{-/-}$ cells (Fig. 3 *A*). Surprisingly, the width of the IFT88 extension toward the BB in *TCTN2*$^{-/-}$ cells was much smaller than that of the IFT88 distribution in cilia. To better understand the location of the narrow extension, we used an EM image and mapped the characteristic structures including the BB, the TZ, and the DAPs onto individual super-resolution images (Fig. 3 *A*). The overlaid images showed that it was likely that the IFT88 extension in *TCTN2*$^{-/-}$ cells was within the BB lumen. To check whether this unexpected finding was IFT88 specific or applicable to other IFT proteins, we examined the localization of IFT144, one of the IFT A proteins, using dSTORM. Similarly, IFT144 proteins also leaked into the BB lumen in some of the TCTN2$^{-/-}$ RPE1 cells, although the intensity was relatively lower (Fig. 3 *B*). We also conducted super-resolution imaging of IFT88 in si-RPGRIP1L RPE1 cells and found that IFT88 of RPGRIP1L-deficient cells shared a phenotypic localization of BB lumen occupancy similar to that of TCTN2$^{-/-}$ cells (Fig. 3 *C*). To examine the average distribution of IFT88 molecules, we overlaid all dSTORM images from the same species into one image by aligning the location of SCLT1 (Fig. 3 *D*), clearly showing the narrow occupancy of IFT88 toward the BB lumen in *TCTN2*$^{-/-}$ cells. The intensity profiles along the ciliary central axis illustrated the IFT88 extension of ∼500 nm (Fig. 3 *E*), which was close to the length of a mammalian BB. The intensity analysis of the images in Fig. 3 *D* in each cross section along the longitudinal direction showed a width of ∼100 nm for the IFT88 extension in terms of the FWHM of the intensity in *TCTN2*$^{-/-}$ cells (Fig. 3 *F*). Furthermore, it showed that the width of the IFT88 distributed above SCLT1 (longitudinal distance to SCLT1 at 100–400 nm) in the cilia of *TCTN2*$^{-/-}$ cells was slightly narrower than that in WT and *FBF1*$^{-/-}$ cilia (Fig. 3 *F*). This may be correlated with the swelling tip of IFT88, where a large population of IFT88 molecules is present, possibly because of impaired retrograde trafficking.

To further confirm the lumen occupancy of IFT88 in the BB of *TCTN2*$^{-/-}$ cells, we compared the widths of the axonemal microtubules and IFT88 in detail using a number of localization events in dSTORM images. Examining the FWHM of AcTub occupancy in a WT cilium, we found that the diameter of the axonemal microtubules was ∼170 nm (Fig. 4 *A*). Based on EM images, the axonemal diameter of a BB is slightly larger than that of a cilium (52,53). The FWHM of IFT88 in a cilium was ∼197 nm (Fig. 4 *B*). That is, statistically, IFT88 molecules localized in the outer face of the axoneme, which was consistent with the localization of IFT trains observed in EM images (e.g., see (54)). In contrast, the FWHM of IFT88 extension toward the BB in *TCTN2*$^{-/-}$ cells was ∼127 nm (Fig. 4 *C*), which was smaller than the diameter of the axonemal microtubules, assuring the lumen occupancy of IFT88 in the TZ-impaired mutant.

CP110 removal is unaffected in *TCTN2*$^{-/-}$ cells, so the leakage is not related to CP110 regulation

Capping of the distal end of the mother centriole by CP110 suppresses primary cilium formation (55). Removal of CP110 cap upon TTBK2 recruitment precedes multiple processes required for growing a mature primary cilium (56). Previous studies show that IFT88 proteins are recruited to the distal end of the mother centriole before CP110 removal (57). Accordingly, we hypothesized that the leakage of IFT88 may be caused by unscheduled removal or mislocalization of CP110 proteins at the *TCTN2*$^{-/-}$ ciliary base. Examining the localization of CP110, we found that there was no significant difference in the percentages of one CP110 signal (ready for ciliogenesis or missing signal) or two CP110 signals (both mother and daughter centrioles were capped) among nonciliated populations in WT and *TCTN2*$^{-/-}$ cells after serum starvation (Fig. 5, *A* and *B*). That is, TCTN2 KO did not alter the

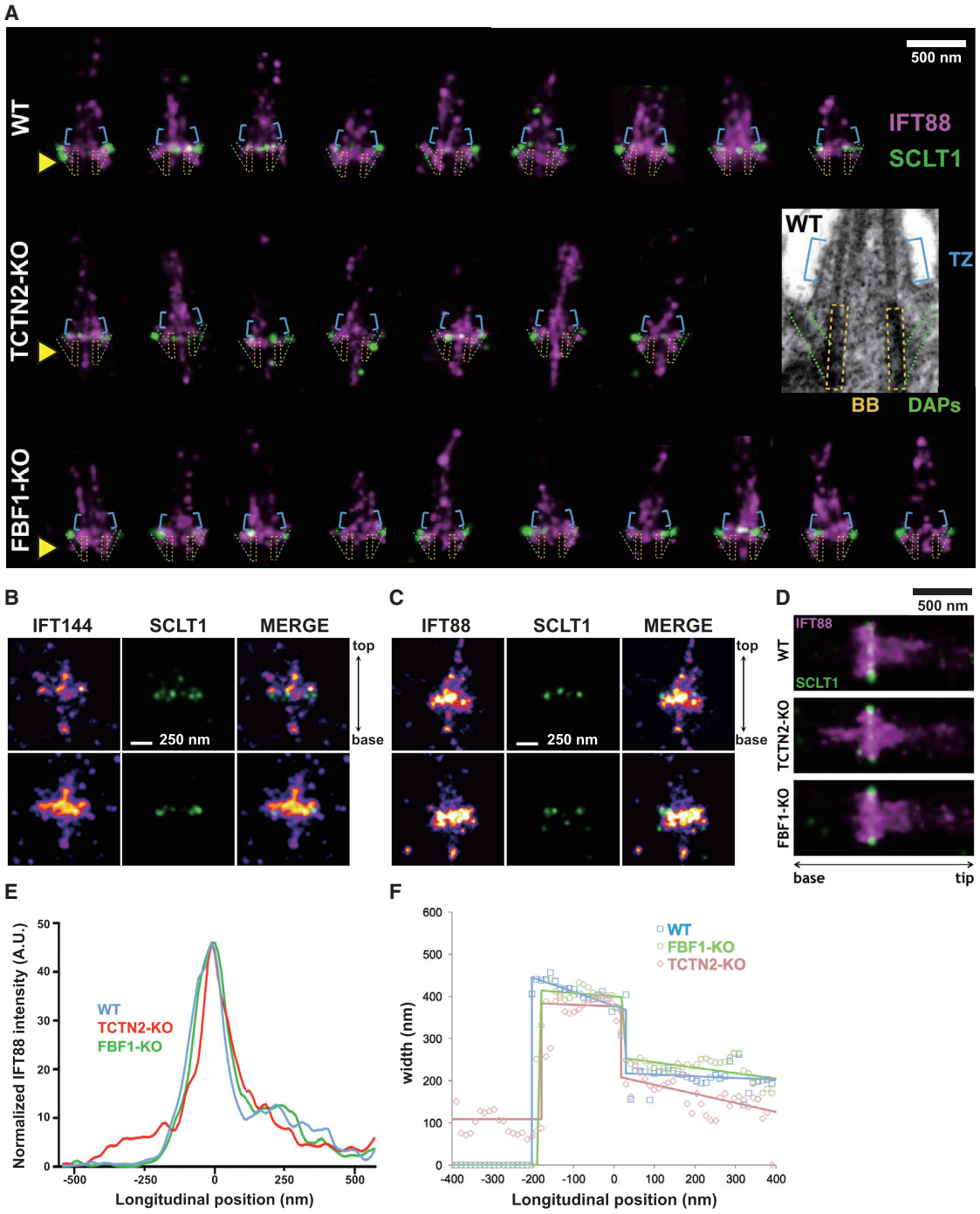

FIGURE 3 Super-resolution microscopy uncovering narrow IFT88 leakage toward the basal body (BB) in *TCTN2*$^{-/-}$ cells. (*A*) IFT88 distributions are shown relative to the distal appendage (DAP) protein SCLT1. IFT88 molecules typically localize to the DAPs, the transition zone (TZ), and the cilium in wild-type (WT) cells. A narrow extension of IFT88 toward the BB (pointed by a *yellow arrowhead*), potentially within the width of the BB axoneme, is observed in each of these representative *TCTN2*$^{-/-}$ cilia. This IFT extension is absent in WT and *FBF1*$^{-/-}$ cilia. Inset: an EM image of a WT RPE1 cell marks the TZ (*blue*), DAPs (*green*), and BB (*yellow*) used to be overlaid in each cilium image for dimensional comparison. (*B*) Extension of IFT144 toward the BB lumen of *TCTN2*$^{-/-}$ RPE1 cells is observed in a single cilium (*upper*) and an overlaid image of multiple cilia (n = 5) (*lower*). (*C*) Extension of IFT88 toward the BB lumen of RPGRIP1L siRNA knockdown cells is shown. (*D*) Overlaid results from the data set in (*A*) show narrow IFT88 leakage into the BB (potentially the BB lumen) in *TCTN2*$^{-/-}$ cells, which is not observed in WT or *FBF1*$^{-/-}$ cells. (*E*) The intensity profiles of (*D*) along the ciliary central axis show the <500 nm IFT88 extension toward the BB in *TCTN2*$^{-/-}$ cells. (*F*) FWHM of the overlaid image in (*D*) at each longitudinal position shows the narrow width of IFT extension toward the BB in *TCTN2*$^{-/-}$ cells. A decreased lateral distribution in the TZ of *TCTN2*$^{-/-}$ cells is also observed. To see this figure in color, go online.

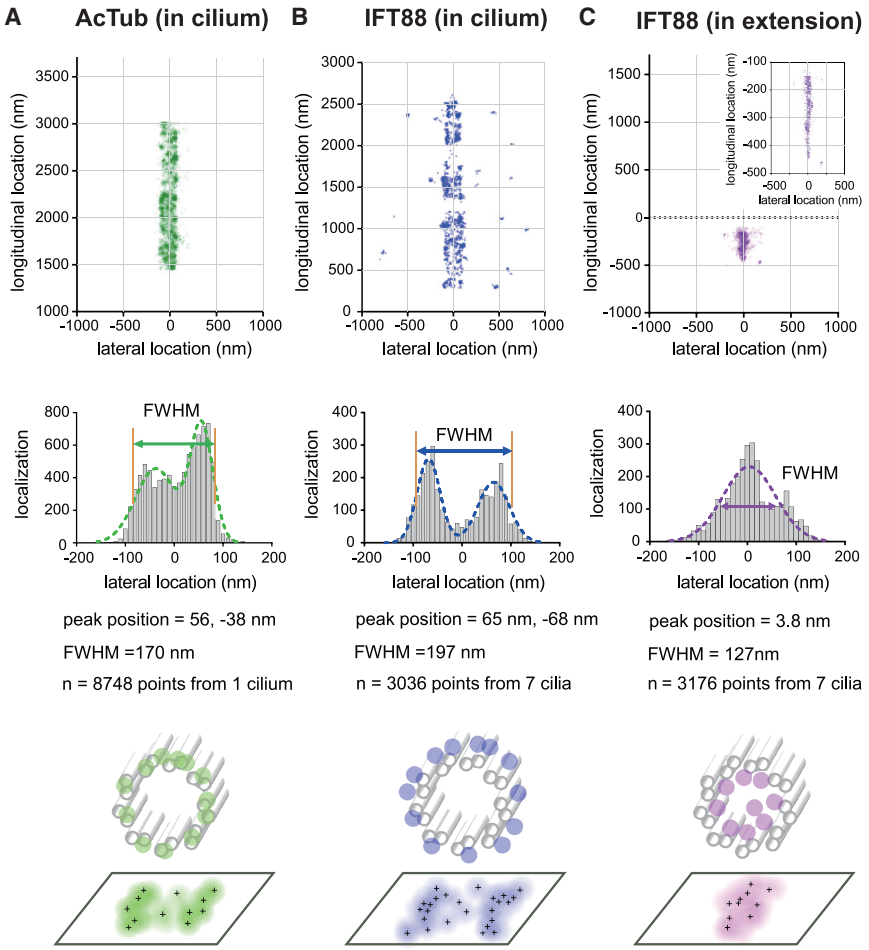

FIGURE 4 Quantitative analysis of super-resolution images confirming the BB lumen occupancy of IFT88 in *TCTN2*$^{-/-}$ cells. The molecular distribution is characterized by systematically measuring its peak position and width in FWHM. The double-peak distributions of AcTub of a wild-type (WT) cilium (*A*) and IFT88 (*B*) in the cilium provide the axoneme diameter and location of IFT88 in the ciliary compartment. (*C*) The FWHM of the width distribution of IFT88 extension toward the BB shows an estimate of ~127 nm in diameter, which is smaller than that of the axoneme. To see this figure in color, go online.

population of CP110 removal. In addition, proximal extension of IFT88 was only observed in ciliated BBs in *TCTN2*$^{-/-}$ cells. Therefore, our results suggest that the capping of proteins such as CP110 at the distal end of the mother centriole may not play a barrier role in preventing proteins from running into the lumen.

Local TZ structural damage is not the cause of IFT88 leakage

As shown above, TCTN2 KO resulted in partial structural damage to the TZ. We thus hypothesized that the IFT leakage may be caused by the TZ structural damage. To test this hypothesis, we tried multiple cell perturbations hoping to find one that could induce the IFT88 extension in WT cells. Intriguingly, we found that Cyto D treatment, which depolymerizes actin and promotes ciliary elongation, triggered IFT88 extension toward the BB in a small population of cells (Fig. 5, *C* and *D*). We found no change on TCTN2 localization after Cyto D treatment (Fig. 5 *E*), which was consistent with previous findings that the TZ structure is unaffected by Cyto D addition (58). This suggests that Cyto-D-induced IFT88 leakage in the small population of WT cells is not related to TZ structure. It has been reported that Cyto-D-induced ciliary elongation is a result of the ciliary recruitment of IFT proteins (Fig. 5 *F*) (58,59). One possibility would be that Cyto-D-enriched IFT particles form a roadblock, resulting in an overflow of IFT88 into the BB lumen. In that case, the TZ structural collapse in *TCTN2*$^{-/-}$ cells could have a similar roadblock effect. If there were a roadblock, there should be an accumulation of IFT88 at the ciliary base. However, we did not find any intensity difference of IFT88 at the ciliary base when treating with Cyto D (Fig. 5 *G*). Meanwhile, transmission EM images did not show obvious axonemal deformation at the TZ region of the *TCTN2*$^{-/-}$ cells (Fig. 5 *H*), suggesting that at least the axonemal structure was unaffected. Collectively, even though TZ is damaged by TCTN2 KO, this damage is not the major cause of IFT88 extension, as found in Cyto D treatment in which IFT extension also occurs with an intact TZ.

Super-resolution imaging reveals structural weakening of TCTN2-depleted cilia

To understand the effect of TZ aberration on the global structure of primary cilia, we performed dSTORM

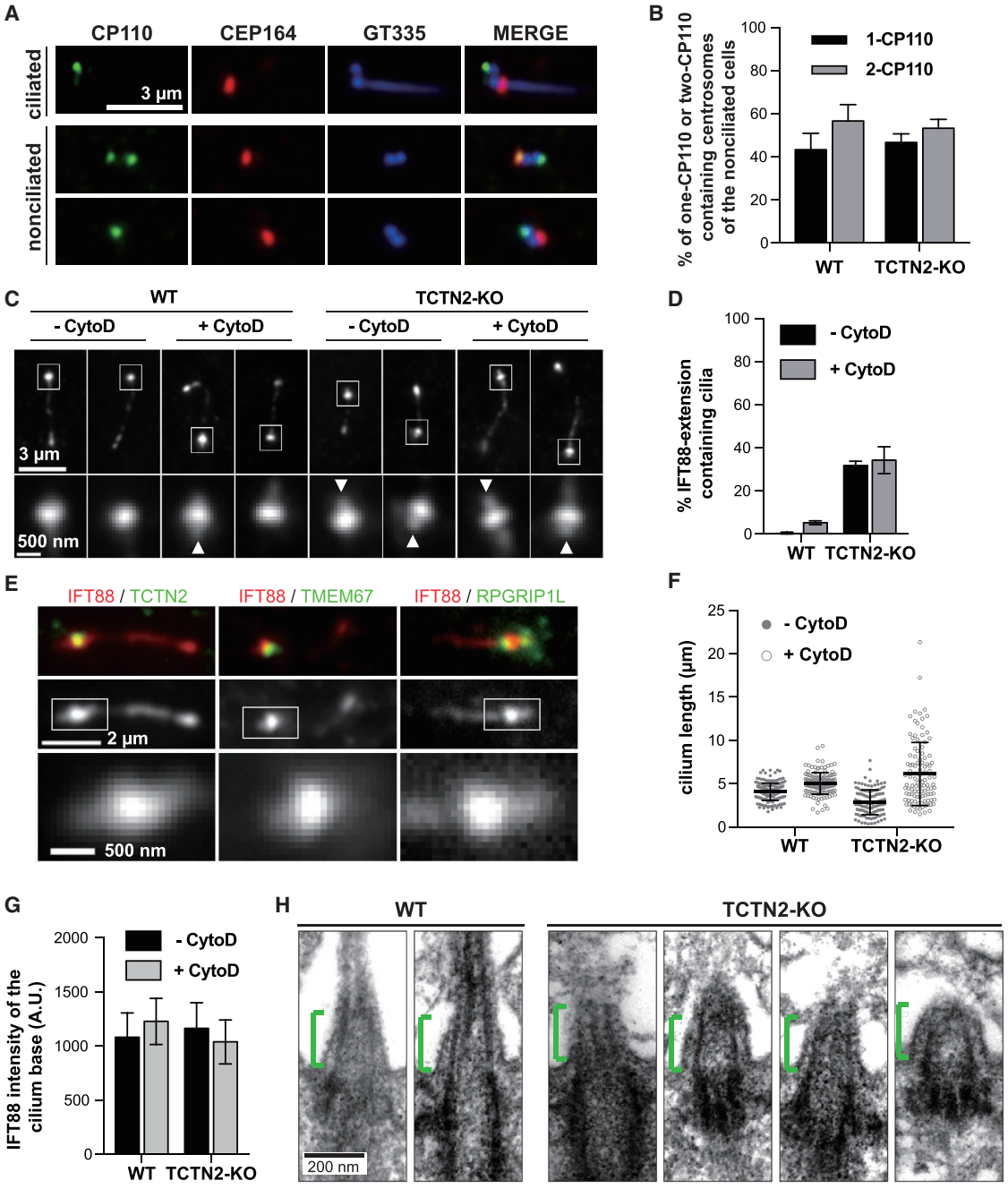

FIGURE 5 Model testing to explain TCTN2 depletion-induced IFT88 leakage into the basal body (BB) lumen. (*A*) CP110 is properly removed from the centriole distal end of *TCTN2*$^{-/-}$ cells as of wild-type (WT) cells, excluding the model of improper CP110 removal for IFT88 leakage. (*B*) Similar proportions of single CP110 centrosomes and double CP110 centrosomes between nonciliated WT and *TCTN2*$^{-/-}$ cells are shown, suggesting a similar efficiency in CP110 removal (N = 3 and n > 50). (*C* and *D*) IFT88 extension into the BB (*C*, *white arrowheads*) is found in a small population of WT cells upon cytochalasin D (Cyto D) treatment. Thus, IFT88 leakage into the BB lumen is not specific to transition zone (TZ) damage. N = 3 and n > 100 for (*D*). (*E*) TZ proteins TCTN2, TMEM67, and RPGRIP1L are intact in Cyto-D-treated WT cells. (*F*) Elongation of WT and *TCTN2*$^{-/-}$ cilia upon Cyto D treatment (n > 100) is shown. (*G*) No significant change in IFT88 intensity is observed at the ciliary base upon Cyto D treatment for both WT and *TCTN2*$^{-/-}$ cells, suggesting no basal accumulation of IFT88 and excluding the traffic jam model for IFT88 leakage (n > 100). (*H*) Transmission electron microscopy shows no structural collapse between the axoneme and the ciliary membrane at the TZ (*green area*), excluding the structural damage model for IFT88 leakage. To see this figure in color, go online.

super-resolution imaging of GT335, a glutamylated tubulin marker, to trace the outlines of axonemes for structural geometry analysis (Fig. 6 *A*). The *TCTN2*$^{-/-}$ cells clearly possessed short and curved cilia when compared to those of WT cells, suggesting that the ciliary growth and rigidity were both affected by TZ damage. To better understand the

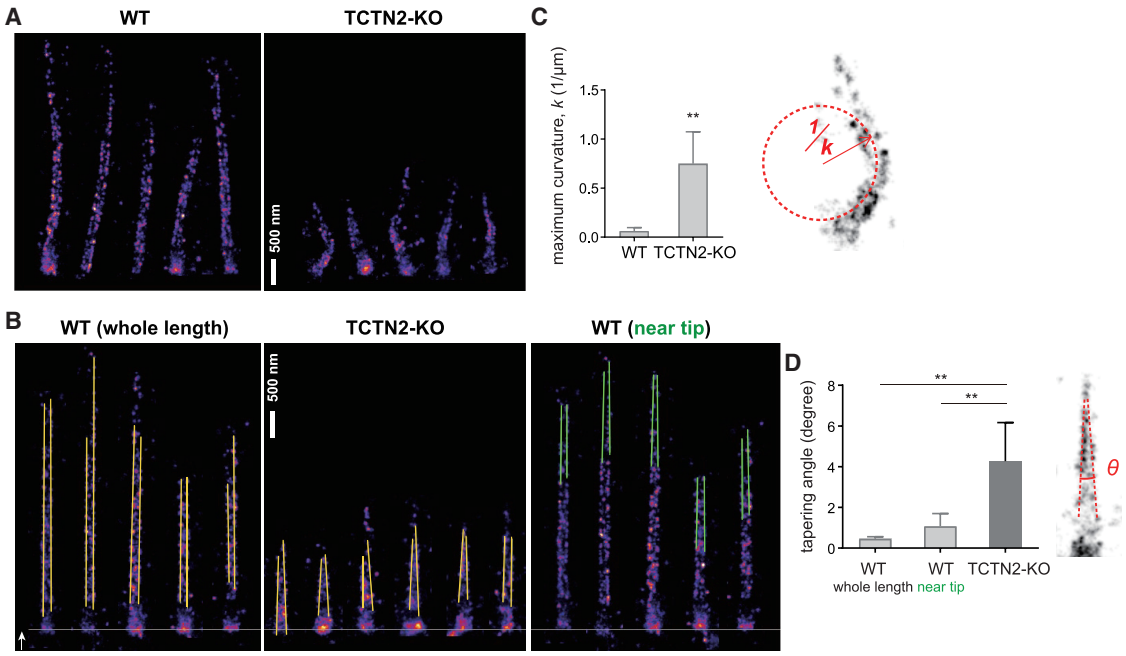

FIGURE 6 Structural weakening of *TCTN2*$^{-/-}$ cilia with a large bending curvature and a large tapering angle. (*A*) Super-resolved images of ciliary marker GT335 reveal two ciliary boundaries in detail for curvature calculation and subsequent flexural rigidity estimation. (*B*) Analysis of the tapering angle of two ciliary boundaries by computationally straightening the ciliary images in (*A*) shows diameter shrinkage of axonemal configuration toward the ciliary tip in *TCTN2*$^{-/-}$ cells. (*C* and *D*) Statistical analysis of the maximal curvature and tapering angle of GT335 pattern for the data set in (*A*) and (*B*) are shown (**$p <$ 0.01 with unpaired *t*-test). To see this figure in color, go online.

geometry of microtubule bundles, we straightened each individual cilium computationally (see Materials and Methods), keeping the width at each cross section unchanged (Fig. 6 *B*). Intriguingly, we found that the microtubules of *TCTN2*$^{-/-}$ cilia were tapered more rapidly than those of WT cilia. That is, when the TZ was impaired, the parallel extension of axonemal microtubules could not be maintained, possibly because of the premature termination of a few of the nine doublets before reaching the ciliary tip or the lack of molecules that maintain a doublet-doublet distance. The curvature analysis showed that the maximal curvature of WT is ~0.06/μm, whereas that of *TCTN2*$^{-/-}$ is ~0.75/μm (Fig. 6 *C*). Based on elastic approximation in mechanics of materials (60), curvature is inversely proportional to the flexural rigidity ($k = -M/EI$, where k is the curvature, M is the bending moment, and EI is the flexural rigidity). Assuming similar environmental conditions of WT and *TCTN2*$^{-/-}$ cilia yielding a similar bending moment in both cases, the bending curvature, which is proportional to the bending moment, should be independent of the ciliary length. Thus, the WT cilia are ~12.5 times more rigid than the *TCTN2*$^{-/-}$ cilia. As shown above that *TCTN2*$^{-/-}$ cilia were not acetylated, our results support a hypothesis in which lack of acetylation can possibly lower the flexural rigidity of cilia, thus increasing ciliary curvature. The average tapering angle of *TCTN2*$^{-/-}$ cilia was ~4.27°, much larger than that of WT cilia, even considering only the tip segment (Fig. 6, *B* and *D*), implying diameter reduction from ~240 nm at the ciliary base to 200 nm at the location 500 nm from the ciliary base, also contributing to the weakening of the ciliary structure.

DISCUSSION

Here, we reveal defects caused by TCTN2 depletion, including partial TZ damage, loss of ciliary membrane protein retention, IFT88 lumen leakage toward the BB, and ciliary structural weakening. Our findings augment the understanding of the molecular mechanisms underlying ciliopathic phenotypes. Consistent with our molecular architecture mapping of the TZ (40), TCTN2 KO affects the nearby TMEM67 and MKS1 but not the distant molecules such as RPGRIP1L and CEP290. The loss of ARL13B and SMO from *TCTN2*$^{-/-}$ cilia is somewhat expected because of the membrane vicinity of TCTN2, reflecting its gating function for membrane proteins. The loss of EHD1, a ciliary pocket protein, may not be directly related to the membrane protein gating. It suggests that TZ destruction may have an effect on cilium-associated endocytic recycling mediated by EHD1. The absence of AcTubs and the presence of glutamylated tubulins in *TCTN2*$^{-/-}$ cilia suggest different TZ regulation of these two posttranslational modification processes. Thus, cilium rigidity is compromised, but microtubule severing protection is maintained.

The BB lumen occupancy of IFT88 in *TCTN2*$^{-/-}$ cilia is a large surprise. Although a recent study has used an image

analysis technique to reveal lumen occupancy of molecular motors and ciliary precursors (61), to the best of our knowledge, no one has reported a direct observation of IFT molecules in the lumen. Here, we show that IFT88 can reach the BB lumen in TZ-damaged cilia. In addition, we also demonstrate the lumen occupancy of IFT88 in WT cilia when treating with Cyto D. Although it remains unclear whether ciliary elongation induced by Cyto D can result in local structural defects, at least we demonstrate that IFT proteins indeed are able to reach the lumen in WT cells under specific conditions.

Multiple models may explain this IFT88 extension toward the BB lumen, i.e., improper CP110 removal model, traffic jam model, structure break model, tip leakage model, and misregulation model. The finding of unaltered single and double CP110 populations in nonciliated WT and TCTN2$^{-/-}$ cells eliminates the improper CP110 removal model. The leakage in WT cilia with an intact TZ when treating with Cyto D and the normal structure shown in EM seem to suggest that even without a structural break, IFT88 can still reach the lumen. The normal brightness of IFT88 at the ciliary base of both *TCTN2*$^{-/-}$ cells and Cyto-D-treated WT cells suggests that no traffic jam occurred, rejecting the traffic jam model. A tip leakage model is possible considering that axonemal tapering of *TCTN2*$^{-/-}$ cilia and abnormal elongation of Cyto-D-treated WT cilia can both form disorganized microtubule bundles toward the ciliary tip. If asymmetric growth of different microtubule doublets occurs, it is possible that the structure is not tight enough to prevent IFT proteins from leaking into the lumen. It remains unclear why these IFT proteins leak all the way to the BB lumen, knowing that some proteins occupy the proximal end of the BB lumen (e.g., C2CD3 (46)). Misregulation of IFT protein passage through the TZ is also a possible scenario for explaining the lumen leakage, although the detailed process is not easy to picture without more experimental tests.

SUPPORTING MATERIAL

Two figures are available at http://www.biophysj.org/biophysj/supplemental/S0006-3495(18)30622-2.

AUTHOR CONTRIBUTIONS

R.R.W. and J.-C.L. designed the research. R.R.W., T.T.Y., and J.-C.L. designed the experiments. R.R.W., T.T.Y., C.-E.H., C.-W.C., and W.-J.W. conducted the experiments. R.R.W., T.T.Y., and J.-C.L. analyzed the data and wrote the article.

ACKNOWLEGEMENTS

The authors thank Bryan Tsou, Barbara Tanos, and Gregory Pazour for providing reagents and Wann-Neng Jane for helping with EM.

This work was supported by the Ministry of Science and Technology, Taiwan (grant number 106-2112-M-001-030), the Academia Sinica Career Development Award, and the National Taiwan University and Academia Sinica Innovative Joint Program (grant number NTU-AS-106R104503).

REFERENCES

1. Singla, V., and J. F. Reiter. 2006. The primary cilium as the cell's antenna: signaling at a sensory organelle. *Science.* 313:629–633.
2. Goetz, S. C., and K. V. Anderson. 2010. The primary cilium: a signalling centre during vertebrate development. *Nat. Rev. Genet.* 11:331–344.
3. Anderson, R. G. 1972. The three-dimensional structure of the basal body from the rhesus monkey oviduct. *J. Cell Biol.* 54:246–265.
4. Andersen, J. S., C. J. Wilkinson, …, M. Mann. 2003. Proteomic characterization of the human centrosome by protein correlation profiling. *Nature.* 426:570–574.
5. Li, J. B., J. M. Gerdes, …, S. K. Dutcher. 2004. Comparative genomics identifies a flagellar and basal body proteome that includes the BBS5 human disease gene. *Cell.* 117:541–552.
6. Nogales-Cadenas, R., F. Abascal, …, A. Pascual-Montano. 2009. CentrosomeDB: a human centrosomal proteins database. *Nucleic Acids Res.* 37:D175–D180.
7. Bornens, M. 2012. The centrosome in cells and organisms. *Science.* 335:422–426.
8. Valenstein, M. L., and A. Roll-Mecak. 2016. Graded control of microtubule severing by tubulin glutamylation. *Cell.* 164:911–921.
9. Portran, D., L. Schaedel, …, M. V. Nachury. 2017. Tubulin acetylation protects long-lived microtubules against mechanical ageing. *Nat. Cell Biol.* 19:391–398.
10. Tanos, B. E., H. J. Yang, …, M. F. Tsou. 2013. Centriole distal appendages promote membrane docking, leading to cilia initiation. *Genes Dev.* 27:163–168.
11. Rosenbaum, J. L., and F. M. Child. 1967. Flagellar regeneration in protozoan flagellates. *J. Cell Biol.* 34:345–364.
12. Boisvieux-Ulrich, E., M. C. Laine, and D. Sandoz. 1989. In vitro effects of taxol on ciliogenesis in quail oviduct. *J. Cell Sci.* 92:9–20.
13. Kozminski, K. G., K. A. Johnson, …, J. L. Rosenbaum. 1993. A motility in the eukaryotic flagellum unrelated to flagellar beating. *Proc. Natl. Acad. Sci. USA.* 90:5519–5523.
14. Rosenbaum, J. L., and G. B. Witman. 2002. Intraflagellar transport. *Nat. Rev. Mol. Cell Biol.* 3:813–825.
15. Gilula, N. B., and P. Satir. 1972. The ciliary necklace. A ciliary membrane specialization. *J. Cell Biol.* 53:494–509.
16. Garcia-Gonzalo, F. R., and J. F. Reiter. 2012. Scoring a backstage pass: mechanisms of ciliogenesis and ciliary access. *J. Cell Biol.* 197:697–709.
17. Reiter, J. F., O. E. Blacque, and M. R. Leroux. 2012. The base of the cilium: roles for transition fibres and the transition zone in ciliary formation, maintenance and compartmentalization. *EMBO Rep.* 13:608–618.
18. Dowdle, W. E., J. F. Robinson, …, J. F. Reiter. 2011. Disruption of a ciliary B9 protein complex causes Meckel syndrome. *Am. J. Hum. Genet.* 89:94–110.
19. Garcia-Gonzalo, F. R., K. C. Corbit, …, J. F. Reiter. 2011. A transition zone complex regulates mammalian ciliogenesis and ciliary membrane composition. *Nat. Genet.* 43:776–784.
20. Sang, L., J. J. Miller, …, P. K. Jackson. 2011. Mapping the NPHP-JBTS-MKS protein network reveals ciliopathy disease genes and pathways. *Cell.* 145:513–528.
21. Chih, B., P. Liu, …, A. S. Peterson. 2011. A ciliopathy complex at the transition zone protects the cilia as a privileged membrane domain. *Nat. Cell Biol.* 14:61–72.
22. Winkelbauer, M. E., J. C. Schafer, …, B. K. Yoder. 2005. The C. elegans homologs of nephrocystin-1 and nephrocystin-4 are cilia

transition zone proteins involved in chemosensory perception. *J. Cell Sci.* 118:5575–5587.

23. Fliegauf, M., J. Horvath, …, H. Omran. 2006. Nephrocystin specifically localizes to the transition zone of renal and respiratory cilia and photoreceptor connecting cilia. *J. Am. Soc. Nephrol.* 17:2424–2433.
24. Williams, C. L., C. Li, …, M. R. Leroux. 2011. MKS and NPHP modules cooperate to establish basal body/transition zone membrane associations and ciliary gate function during ciliogenesis. *J. Cell Biol.* 192:1023–1041.
25. Huang, L., K. Szymanska, …, K. M. Boycott. 2011. TMEM237 is mutated in individuals with a Joubert syndrome related disorder and expands the role of the TMEM family at the ciliary transition zone. *Am. J. Hum. Genet.* 89:713–730.
26. Craige, B., C. C. Tsao, …, G. B. Witman. 2010. CEP290 tethers flagellar transition zone microtubules to the membrane and regulates flagellar protein content. *J. Cell Biol.* 190:927–940.
27. Shi, X., G. Garcia, III, …, J. F. Reiter. 2017. Super-resolution microscopy reveals that disruption of ciliary transition-zone architecture causes Joubert syndrome. *Nat. Cell Biol.* 19:1178–1188.
28. Wang, W.-J., H. G. Tay, …, M. F. Tsou. 2013. CEP162 is an axoneme-recognition protein promoting ciliary transition zone assembly at the cilia base. *Nat. Cell Biol.* 15:591–601.
29. Li, C., V. L. Jensen, …, M. R. Leroux. 2016. MKS5 and CEP290 dependent assembly pathway of the ciliary transition zone. *PLoS Biol.* 14:e1002416.
30. Reiter, J. F., and W. C. Skarnes. 2006. Tectonic, a novel regulator of the Hedgehog pathway required for both activation and inhibition. *Genes Dev.* 20:22–27.
31. Shaheen, R., E. Faqeih, …, F. S. Alkuraya. 2011. A TCTN2 mutation defines a novel Meckel Gruber syndrome locus. *Hum. Mutat.* 32:573–578.
32. Yee, L. E., F. R. Garcia-Gonzalo, …, J. F. Reiter. 2015. Conserved genetic interactions between ciliopathy complexes cooperatively support ciliogenesis and ciliary signaling. *PLoS Genet.* 11:e1005627.
33. Dishinger, J. F., H. L. Kee, …, K. J. Verhey. 2010. Ciliary entry of the kinesin-2 motor KIF17 is regulated by importin-β2 and RanGTP. *Nat. Cell Biol.* 12:703–710.
34. Hu, Q., L. Milenkovic, …, W. J. Nelson. 2010. A septin diffusion barrier at the base of the primary cilium maintains ciliary membrane protein distribution. *Science.* 329:436–439.
35. Kee, H. L., J. F. Dishinger, …, K. J. Verhey. 2012. A size-exclusion permeability barrier and nucleoporins characterize a ciliary pore complex that regulates transport into cilia. *Nat. Cell Biol.* 14:431–437.
36. Nachury, M. V., E. S. Seeley, and H. Jin. 2010. Trafficking to the ciliary membrane: how to get across the periciliary diffusion barrier? *Annu. Rev. Cell Dev. Biol.* 26:59–87.
37. Yang, T., M. N. T. Tran, …, J.-C. Liao. 2017. Intraflagellar transport proteins undergo nonaxonemal staged hindrance between the recruiting distal appendages and the cilium. *bioRxiv* https://doi.org/10.1101/227587.
38. Jensen, V. L., C. Li, …, M. R. Leroux. 2015. Formation of the transition zone by Mks5/Rpgrip1L establishes a ciliary zone of exclusion (CIZE) that compartmentalises ciliary signalling proteins and controls PIP2 ciliary abundance. *EMBO J.* 34:2537–2556.
39. Weatherbee, S. D., L. A. Niswander, and K. V. Anderson. 2009. A mouse model for Meckel syndrome reveals Mks1 is required for ciliogenesis and Hedgehog signaling. *Hum. Mol. Genet.* 18:4565–4575.
40. Yang, T. T., J. Su, …, J. C. Liao. 2015. Superresolution pattern recognition reveals the architectural map of the ciliary transition zone. *Sci. Rep.* 5:14096.
41. Vieillard, J., M. Paschaki, …, B. Durand. 2016. Transition zone assembly and its contribution to axoneme formation in Drosophila male germ cells. *J. Cell Biol.* 214:875–889.
42. Lambacher, N. J., A. L. Bruel, …, O. E. Blacque. 2016. TMEM107 recruits ciliopathy proteins to subdomains of the ciliary transition zone and causes Joubert syndrome. *Nat. Cell Biol.* 18:122–131.
43. Yang, T. T., P. J. Hampilos, …, J. C. Liao. 2013. Superresolution STED microscopy reveals differential localization in primary cilia. *Cytoskeleton (Hoboken).* 70:54–65.
44. Mali, P., L. Yang, …, G. M. Church. 2013. RNA-guided human genome engineering via Cas9. *Science.* 339:823–826.
45. Heigwer, F., G. Kerr, and M. Boutros. 2014. E-CRISP: fast CRISPR target site identification. *Nat. Methods.* 11:122–123.
46. Yang, T. T., W. M. Chong, …, J. C. Liao. 2018. Super-resolution architecture of mammalian centriole distal appendages reveals distinct blade and matrix functional elements. *Nat. Commun.* 9:2023.
47. Larkins, C. E., G. D. Aviles, …, T. Caspary. 2011. Arl13b regulates ciliogenesis and the dynamic localization of Shh signaling proteins. *Mol. Biol. Cell.* 22:4694–4703.
48. Mariani, L. E., M. F. Bijlsma, …, T. Caspary. 2016. Arl13b regulates Shh signaling from both inside and outside the cilium. *Mol. Biol. Cell.* 27:3780–3790.
49. Rohatgi, R., L. Milenkovic, and M. P. Scott. 2007. Patched1 regulates hedgehog signaling at the primary cilium. *Science.* 317:372–376.
50. Lu, Q., C. Insinna, …, C. J. Westlake. 2015. Early steps in primary cilium assembly require EHD1/EHD3-dependent ciliary vesicle formation. *Nat. Cell Biol.* 17:228–240.
51. Bhattacharyya, S., M. A. Rainey, …, H. Band. 2016. Endocytic recycling protein EHD1 regulates primary cilia morphogenesis and SHH signaling during neural tube development. *Sci. Rep.* 6:20727.
52. Molla-Herman, A., R. Ghossoub, …, A. Benmerah. 2010. The ciliary pocket: an endocytic membrane domain at the base of primary and motile cilia. *J. Cell Sci.* 123:1785–1795.
53. Li, S., J. J. Fernandez, …, D. A. Agard. 2012. Three-dimensional structure of basal body triplet revealed by electron cryo-tomography. *EMBO J.* 31:552–562.
54. Vannuccini, E., E. Paccagnini, …, P. Lupetti. 2016. Two classes of short intraflagellar transport train with different 3D structures are present in Chlamydomonas flagella. *J. Cell Sci.* 129:2064–2074.
55. Spektor, A., W. Y. Tsang, …, B. D. Dynlacht. 2007. Cep97 and CP110 suppress a cilia assembly program. *Cell.* 130:678–690.
56. Goetz, S. C., K. F. Liem, Jr., and K. V. Anderson. 2012. The spinocerebellar ataxia-associated gene Tau tubulin kinase 2 controls the initiation of ciliogenesis. *Cell.* 151:847–858.
57. Sedmak, T., and U. Wolfrum. 2011. Intraflagellar transport proteins in ciliogenesis of photoreceptor cells. *Biol. Cell.* 103:449–466.
58. Fu, W., L. Wang, …, B. D. Dynlacht. 2016. Role for the IFT-A complex in selective transport to the primary cilium. *Cell Reports.* 17:1505–1517.
59. Kim, J., J. E. Lee, …, J. G. Gleeson. 2010. Functional genomic screen for modulators of ciliogenesis and cilium length. *Nature.* 464:1048–1051.
60. Gere, J. M., and S. Timoshenko. 2001. Mechanics of Materials. Brooks. Cole, Pacific Grove, CA, pp. 815–839.
61. Luo, W., A. Ruba, …, W. Yang. 2017. Axonemal lumen dominates cytosolic protein diffusion inside the primary cilium. *Sci. Rep.* 7:15793.

Biophysical Journal, Volume *115*

Supplemental Information

Super-Resolution Imaging Reveals TCTN2 Depletion-Induced IFT88 Lumen Leakage and Ciliary Weakening

Rueyhung Roc Weng, T. Tony Yang, Chia-En Huang, Chih-Wei Chang, Won-Jing Wang, and Jung-Chi Liao

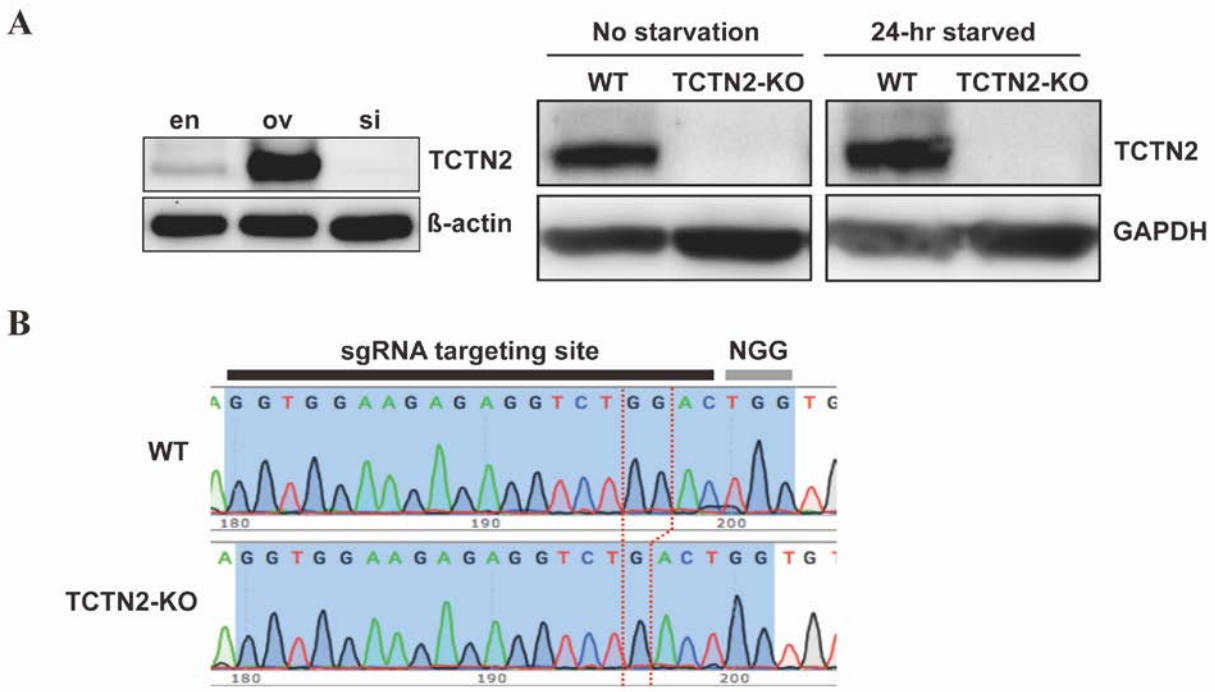

Figure S1. Validation of overexpression and depletion of TCTN2. (*A*) Immunoblotting of cells expressing endogenous (en), overexpressed (ov) and siRNA knockdown (si) of TCTN2 confirmed the effectiveness of antibody specificity, plasmid for overexpression and siRNA knockdown. CRISPR/Cas9 knockout (KO) efficiency is also verified. (*B*) A sequencing result showing loss of a guanine at the sgRNA targeting site of *TCTN2*$^{-/-}$ RPE1 cells.

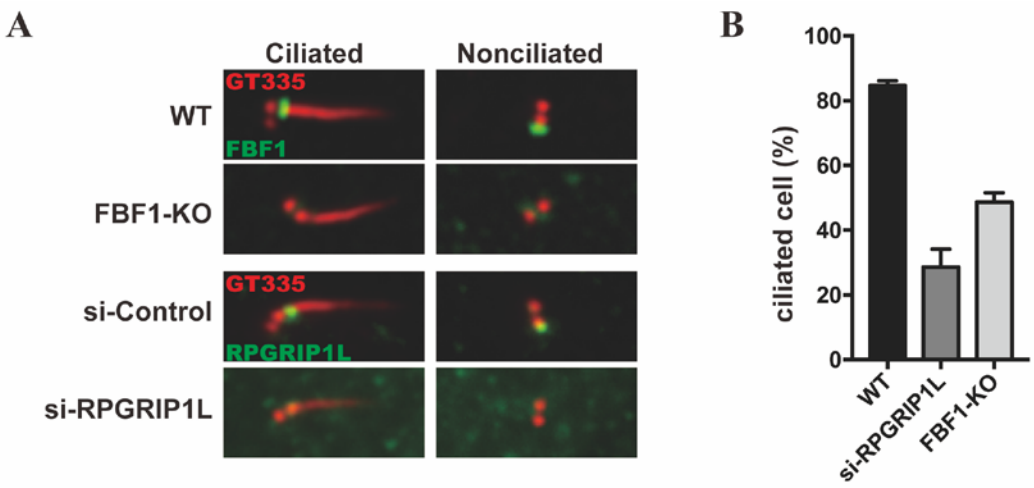

Figure S2. Validation of RPGRIP1L knockdown and FBF1 knockout efficiencies. (*A*) Immunostained images confirming the effectiveness of *RPGRIP1L* siRNA knockdown and *FBF1* CRISPR/Cas9 knockout. (*B*) Reduction of ciliation frequency by RPGRIP1L knockdown and FBF1 knockout.